Variability of the thermal conductance of gold-alkane-gold single-molecule junctions studied using ab-initio and molecular dynamics approaches

J. C. Klöckner[1,2] and F. Pauly[1,2*]
[1] *Okinawa Institute of Science and Technology Graduate University, Onna-son, Okinawa 904-0495, Japan and*
[2] *Department of Physics, University of Konstanz, D-78457 Konstanz, Germany*

Motivated by recent experiments, we study the variability of the thermal conductance of single dithiolated alkane molecules of varying length connecting two gold electrodes. For this purpose, we examine (i) the influence of the metal-molecule contact and of the electrode orientation on the thermal conductance of straight alkane chains, (ii) the effect of molecule-internal disorder realized through torsional gauche defects and the behavior upon stretching, and (iii) the modifications resulting from temperature-dependent dynamical variations of the geometry. While we analyze the former two aspects with a combination of density functional theory (DFT) and nonequilibrium Green's function (NEGF) methods, in the latter case we use nonequilibrium molecular dynamics (NEMD). Our calculations show the size of the variation of the phonon thermal conductance due to changes in contact geometry, that gauche defects generally reduce the thermal conductance but that they vanish upon stretching of the junction, and that the thermal conductance at elevated temperatures results from an average over many junction configurations, including alkanes with thermally excited gauche defects. Overall we find a good agreement between the DFT-NEGF and NEMD approaches for our room-temperature investigations. This confirms that anharmonic effects do not play a major role in alkane chains containing between four to ten carbon atoms. The phonon heat transport thus proceeds elastically and phase-coherently through these short molecular junctions.

I. INTRODUCTION

Since the pioneering theoretical proposal of a rectifying single-molecule device [1] and the first charge transport measurements on single molecules [2, 3], many groundbreaking experiments have explored fundamental physical aspects in these kinds of nanojunctions. They involve the electrical conductance [4, 5], thermoelectricity [6, 7], energy dissipation [8], quantum interference [9, 10] and electronic noise [11–13]. All of these studies contributed significantly to our current understanding of the phase-coherent electronic charge transport at the nanoscale, thereby establishing the active research field of molecular electronics [14–16]. One of the most appealing features of molecular junctions is their tunability in terms of chemical synthesis, including molecular length [17], conjugation [18, 19], anchoring groups [20, 21], and chemical substituents [22], as well as the possibility to exert external control, for instance through mechanical forces [23, 24] or photons to trigger optically induced switching [25].

Only recently the molecular junctions have been pushed into an entirely new direction by measuring their thermal conductance [26]. Since most molecules exhibit a rather insulating, off-resonant charge transport behavior, electronic contributions to the thermal conductance can typically be disregarded [26–28]. The thermal conductance thus arises basically from phonons or photons [29]. Due to the recently established measurement scheme of self-breaking single-molecule junctions [26], which will be described further below, radiative heat transport plays no role, and the phononic thermal conductance contribution is directly determined. This allows to explore the physics of bosonic quasiparticles at the nanoscale. Similar to the field of "molecular electronics" the upcoming field of "molecular nanophononics" will benefit from the molecular tunability. Theoretical suggestions have already been made to realize interference effects or to adjust the thermal transport by use of anchoring groups and substituents [27, 28, 30–32]. With the novel measurement techniques [26], the theoretical predictions are now amenable to the experimental test.

The thermal transport through self-assembled monolayers of alkane molecules has been studied by several research groups [33–35]. Genuine single-molecule experiments eliminate crucial uncertainties of such ensemble measurements, for example the number of molecules contacted, the role of intermolecular interactions, possible defects in the self-assembled monolayers or thickness variations due to surface corrugation. Ref. [26] has successfully demonstrated room-temperature measurements of the thermal conductance of gold-alkane-gold single-molecule contacts. By detecting a length-independent thermal conductance for dithiolated alkanes of different lengths at room temperature, a basic fingerprint of the phase-coherent nature of heat transport in these nanojunctions has been shown.

The key experimental challenge that has been overcome in Ref. [26] is the detection of minute thermal currents through single-molecule junctions at room temperature. Depending on the applied temperature difference, thermal currents are on the order of picowatts, and a highly sensitive thermal measurement scheme is needed that additionally ensures a high mechanical device stability at the elevated temperatures. In order to measure the thermal conductance at room temperature, the fol-

* Fabian.Pauly@oist.jp

lowing advanced protocol has been developed: In a first step, molecular junctions are characterized electronically through a conventional electrical conductance histogram. The information contained in the histogram is then used to identify single-molecule junctions through the most probable single-molecule electrical conductance. Electrical conductance-distance traces are now taken, but the tip withdrawal is stopped, if a single-molecule junction is identified. At this point the electrical conductance and the temperature of the tip, from which the thermal conductance of the junction can be deduced, are monitored simultaneously. After a waiting time on the order of seconds, the contact finally breaks spontaneously. Due to the low thermal signal, a sophisticated averaging scheme needs to be applied. Several hundred thermal conductance-time traces, each 1.1 s in length, are aligned to the breaking point, identified by the electrical conductance signal, and averaged. In this way a clear change in the thermal conductance due to contact rupture is observed, which is identical to the sum of the phononic and often negligible electronic thermal conductance of the single-molecule junction.

While it would be desirable to measure a full thermal conductance-distance trace, similar to what is possible in electrical conductance measurements, with the newly developed protocol the single-molecule thermal conductance can only be studied at the point of breaking. On the other hand, it is a clear advantage that the measurement protocol determines the thermal conductance as a difference of thermal conductances before and after the thermally induced contact rupture. Since the electrode separation remains unchanged, radiative thermal conductance contributions cancel out. In Ref. [26] the alkane chains C2-C10, containing two to ten carbon atoms, have been analyzed. For C2 the electronic contribution to the thermal conductance was significant, but it could be neglected for C4-C10. For these reasons we focus here on phonon thermal conductance calculations for C4-C10. As the experiment determines the phononic thermal conductance as a mean value over a time series of junction structures before contact rupture, it is important to theoretically explore the magnitude of geometry-induced variations of the thermal conductance. We address this topic in the present work.

Our study is structured as follows. We commence with a description of the theoretical methods in Sec. II, where we introduce the DFT-NEGF method for phonon transport in Sec. II A and the NEMD approach in Sec. II B. The results are presented in Sec. III. In particular, Sec. III A deals with different absorption sites of the alkanedithiols on the electrodes and different electrode orientations. Next, we investigate the influence of gauche defects on transport in Sec. III B and how they respond to strain. Sec. III C adds an analysis of temperature effects via the NEMD approach to the previous two DFT-NEGF studies. We close with the conclusions in Sec. IV.

II. THEORETICAL METHODS

In order to give a comprehensive picture, we take advantage of two complementary approaches to calculate the thermal conductance of single-molecule junctions. To be precise, we first study the phase-coherent phonon transport in the spirit of the Landau-Büttiker scattering theory using NEGF techniques, where the device-specific parameters are obtained from DFT as implemented by us and described in Refs. [36, 37]. The phonon thermal conductance of the nanoconstriction is calculated as a linear-response property based on the harmonic approximation. Anharmonic scattering, for instance from phonon-phonon interactions, is explicitly neglected, and the geometries are obtained as energetically favorable configurations at temperature $T = 0$.

These studies are complemented by NEMD simulations. In comparison to the ab-initio approach, this method offers several advantages. NEMD naturally considers the nonequilibrium situation and temperature gradients inside the junction, i.e., the heat transport can be described for high applied temperature differences between left and right electrodes. Since the experiments measure the thermal conductance in the linear-response regime [26], this is not relevant however, and we apply NEMD and DFT-NEGF in that limit. Whereas the DFT-NEGF methodology is restricted to a few hundreds of atoms for practical computational efforts, with the molecular dynamics (MD) simulations atom numbers on the order of many thousands can easily be handled. Importantly, anharmonic effects are taken into account in a non-perturbative manner. These anharmonic effects lead to phonon-phonon interactions or the temperature-dependent lattice expansion. The time-dependent simulations imply a sampling of the geometrical phase space. The major drawback can be seen in the need for empirical interatomic potentials, which are not universal and often optimized for special purposes. This becomes most evident, when interface structures are considered at the atomic scale. Due to lack of chemical information conventional potentials then tend to fail to describe geometries reliably. Although there are improved potentials, they come along with higher computational costs. In contrast, DFT-based methods are known to provide reliable geometries at atomic scales. Since MD uses classical statistics, another disadvantage is that quantum effects are not taken into account. This limits the applicability to thermal energies above the material-specific highest phonon energies. For gold, our DFT calculations yield a cutoff at around 20 meV, which is on the order of the Debye energy of 15 meV. This corresponds to temperatures above around 200 K, justifying the application in this work.

In short, DFT-NEGF and NEMD approaches complement each other. Therefore both will be used in our room-temperature study. In the following, we will present them in greater detail.

A. Phonon transport in the Landau-Büttiker scattering theory using DFT parameters

For the calculation of heat transport via phonons in the phase-coherent regime, we consider the Hamiltonian due to small displacements $\{Q_\xi\}$ of atoms away from their equilibrium position $\{R_\xi^{(0)}\}$

$$\hat{H} = \frac{1}{2}\sum_\xi \hat{p}_\xi^2 + \frac{1}{2\hbar^2}\sum_{\xi\chi}\hat{q}_\xi K_{\xi\chi}\hat{q}_\chi. \tag{1}$$

In this expression we have introduced the mass-weighted displacement operators $\hat{q}_\xi = \sqrt{M_\xi}\hat{Q}_\xi$ and the mass-scaled momentum operators $\hat{p}_\xi = \hat{P}_\xi/\sqrt{M_\xi}$. They obey the usual commutation relations: $[\hat{q}_\xi, \hat{p}_\chi] = \mathrm{i}\hbar\delta_{\xi\chi}$ and $[\hat{q}_\xi, \hat{q}_\chi] = [\hat{p}_\xi, \hat{p}_\chi] = 0$, where $\xi = (j, c)$ denotes a Cartesian component $c = x, y, z$ of atom j at position $\vec{R}_j = \vec{R}_j^{(0)} + \vec{Q}_j$. As the system-specific quantity we calculate the dynamical matrix $K_{\xi\chi} = \hbar^2\partial^2_{\xi\chi}E_{\mathrm{DFT}}/\sqrt{M_\xi M_\chi}$ as the mass-weighted second derivative of the DFT total ground state energy E_{DFT} with respect to the Cartesian atomic coordinates.

For the transport calculation we divide the dynamical matrix into different subsystems, namely a central (C) scattering region and the two semi-infinite left (L) and right (R) electrodes

$$\boldsymbol{K} = \begin{pmatrix} \boldsymbol{K}_{\mathrm{LL}} & \boldsymbol{K}_{\mathrm{LC}} & \boldsymbol{0} \\ \boldsymbol{K}_{\mathrm{CL}} & \boldsymbol{K}_{\mathrm{CC}} & \boldsymbol{K}_{\mathrm{CR}} \\ \boldsymbol{0} & \boldsymbol{K}_{\mathrm{RC}} & \boldsymbol{K}_{\mathrm{RR}} \end{pmatrix}. \tag{2}$$

In our implementation we extract the elements $\boldsymbol{K}_{X\mathrm{C}}, \boldsymbol{K}_{\mathrm{C}X}, \boldsymbol{K}_{\mathrm{CC}}$ with $X = \mathrm{L,R}$ from an extended central cluster, while the elements $\boldsymbol{K}_{\mathrm{LL}}$ are obtained from a separate bulk calculation. To account for the acoustic sum rule $K_{jc,jc'} = -\sum_{j'\neq j} K_{jc,j'c'}\sqrt{M_{j'}/M_j}$, where j, j' indicate atoms and c, c' Cartesian components, we correct the surface elements as described in Ref. [37]. Since we assume a vanishing coupling between the two leads, the thermal conductance can be calculated as the linear-response coefficient in a heat current formula [38–40] and reads

$$\kappa_{\mathrm{pn}}(T) = \frac{1}{h}\int_0^\infty E\tau_{\mathrm{pn}}(E)\frac{\partial n(E,T)}{\partial T}\mathrm{d}E. \tag{3}$$

Here $n(E,T) = [\exp(E/k_{\mathrm{B}}T) - 1]^{-1}$ represents the Bose function and $\tau_{\mathrm{pn}}(E)$ is the phonon transmission function. In the framework of NEGF it is given by [36, 39]

$$\tau_{\mathrm{pn}}(E) = \mathrm{Tr}\left[\boldsymbol{D}^{\mathrm{r}}_{\mathrm{CC}}(E)\boldsymbol{\Lambda}_{\mathrm{L}}(E)\boldsymbol{D}^{\mathrm{a}}_{\mathrm{CC}}(E)\boldsymbol{\Lambda}_{\mathrm{R}}(E)\right], \tag{4}$$

where $\boldsymbol{D}^{\mathrm{r,a}}_{\mathrm{CC}}(E)$ are the retarded and advanced phonon Green's functions of the center. They are defined as $\boldsymbol{D}^{\mathrm{a}}_{\mathrm{CC}}(E) = \boldsymbol{D}^{\mathrm{r}}_{\mathrm{CC}}(E)^\dagger$ and

$$\boldsymbol{D}^{\mathrm{r}}_{\mathrm{CC}}(E) = \left[(E+i\eta)^2\,\boldsymbol{1}_{\mathrm{CC}} - \boldsymbol{K}_{\mathrm{CC}} - \boldsymbol{\Pi}^{\mathrm{r}}_{\mathrm{L}}(E) - \boldsymbol{\Pi}^{\mathrm{r}}_{\mathrm{R}}(E)\right]^{-1} \tag{5}$$

with the infinitesimal parameter $\eta > 0$. The scattering rate matrices

$$\boldsymbol{\Lambda}_X(E) = i\left[\boldsymbol{\Pi}^{\mathrm{r}}_X(E) - \boldsymbol{\Pi}^{\mathrm{a}}_X(E)\right] \tag{6}$$

are related to the corresponding embedding self-energies

$$\boldsymbol{\Pi}^{\mathrm{r}}_X(E) = \boldsymbol{K}_{\mathrm{C}X}\boldsymbol{d}^{\mathrm{r}}_{XX}(E)\boldsymbol{K}_{X\mathrm{C}}, \tag{7}$$

which describe the coupling between the C region and electrode X. In the expressions $\boldsymbol{\Pi}^{\mathrm{a}}_X(E) = \boldsymbol{\Pi}^{\mathrm{r}}_X(E)^\dagger$ and $\boldsymbol{d}^{\mathrm{r}}_{XX}(E) = [(E+i\eta)^2\boldsymbol{1}_{XX} - \boldsymbol{K}_{\mathrm{XX}}]^{-1}$ is the surface Green's function of lead $X = \mathrm{L,R}$, which we calculate using the decimation technique explained in Refs. [41, 42].

To better understand heat transport, we consider the decomposition of the total phonon transmission of Eq. (4) into contributions of transmission eigenchannels, $\tau_{\mathrm{pn}}(E) = \sum_i \tau_{\mathrm{pn},i}(E)$. The coefficients $\tau_{\mathrm{pn},i}(E)$ are the eigenvalues of the phonon transmission probability matrix $\boldsymbol{t}_{\mathrm{pn}}(E)\boldsymbol{t}^\dagger_{\mathrm{pn}}(E)$, where $\boldsymbol{t}_{\mathrm{pn}}(E) = \boldsymbol{\Lambda}^{1/2}_{\mathrm{R}}(E)\boldsymbol{D}^{\mathrm{r}}_{\mathrm{CC}}(E)\boldsymbol{\Lambda}^{1/2}_{\mathrm{L}}(E)$ is the phonon transmission amplitude matrix. In this way on gets insight into the number of eigenchannels, which are important for heat transport at a specific energy, and a visualization of the transmission eigenchannels yields information on how the vibrational energy is transported through the nanojunctions. For a detailed discussion of the methodology, we refer to Ref. [43].

Another useful quantity is the cumulative thermal conductance

$$\kappa^{\mathrm{c}}_{\mathrm{pn}}(E,T) = \frac{1}{h}\int_0^E E'\tau_{\mathrm{ph}}(E')\frac{\partial n(E',T)}{\partial T}\mathrm{d}E', \tag{8}$$

defined as the thermal conductance at temperature T due to phonon modes up to the given energy E. It provides information on how vibrational modes contribute to the total thermal conductance.

For the DFT calculations we use TURBOMOLE V7.1 [44–46], employ the Perdew-Burke-Ernzerhof PBE exchange-correlation functional [47, 48] and the default2 basis set of split-valence-plus-polarization quality def2-SV(P) [49] together with the corresponding Coulomb fitting basis [50]. In order to accurately determine the vibrational energies and force constants, we use very strict convergence criteria. In particular, total energies are converged to a precision of better than 10^{-9} a.u., whereas geometry optimizations are performed until the change of the maximum norm of the Cartesian gradient is below 10^{-5} a.u.. For the transmission calculations we use 32×32 k-points transverse to the direction of transport and $\eta = 10^{-5}$ a.u..

B. Phonon transport in NEMD

As an alternative to the calculation of the thermal conductance based on the DFT-NEGF methodology, MD offers different possibilities to predict the heat current at

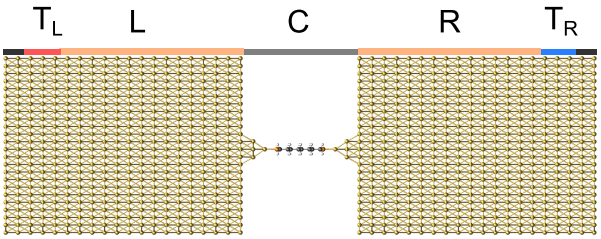

FIG. 1. Geometry used in the NEMD simulations. The outermost atoms (marked by a black line above the corresponding atomic planes) are fixed to prevent a collapse of the system. They are followed by the atoms that are connected to the thermostats (red and blue) and held at constant temperatures of T_{L} and T_{R}. The flexible electrode reservoir atoms (orange) on the left (L) and right (R) are bridged by a central (C) junction part (gray), containing gold tip structures and the alkane molecule.

the atomistic level. Generally speaking, the MD methods can be classified into two different subgroups, namely equilibrium MD and NEMD [51]. While in equilibrium MD one computes transport properties from correlation functions using the Green-Kubo formalism, in NEMD the system is driven out of equilibrium and the response is calculated directly. In principle, with either method both bulk [51–53] and interface [54–57] thermal conductivities can be calculated. However, all of the MD methods require a certain minimal amount of atoms to avoid finite-size effects [58–60].

In this work we use a direct NEMD approach, where the nonequilibrium situation is realized by maintaining two spatially separated regions at a constant temperature difference using thermostats, see Fig. 1. Our simulations are done with the LAMMPS software code [61].

A crucial factor in MD simulations is the choice of the interatomic interaction potentials. Calculations of heat transfer through hybrid metal-organic interfaces have used a Morse potential to describe the sulfur-gold bond [62, 63]. This kind of parametrization is useful to characterize the binding situation in a self-assembled monolayer [62, 64, 65]. In single-molecule junctions, however, we find that these potentials are incapable of describing the chemical bond at the metal-molecule contact correctly but lead to an overcoordination at the sulfur atom, which tends to bind to too many gold atoms. Additionally, covalent intramolecular interactions are often treated in the harmonic approximation [62–65]. In this work, we employ a reactive force field (REAXFF) [66, 67], which is based on the concept of bond order to model bonded and non-bonded interactions between atoms. Importantly, it can describe both bond breaking and bond formation, and all interatomic interactions in the systems are anharmonic.

Figure 1 shows a starting geometry of our NEMD simulations. We employ periodic boundary conditions perpendicular to the direction of transport and fixed boundary conditions parallel to it. The outermost atoms on each side, indicated by the black line above the geometry, are held fixed to avoid a collapse of the system. These regions are followed by several atom rows, marked by the red and blue lines, where thermostats are applied that keep these regions at constant temperatures. In detail we use two velocity rescale thermostats (with *fraction* factor $\alpha = 0.8$ und *window*$= 0.01$ K) to maintain temperatures at T_{L} and T_{R}, as described in Ref. [68]. The largest part of the simulation box consists of the L and R electrode atoms, indicated by the orange lines. To avoid finite-size effects, we have included in these regions so many atoms, that the phononic density of states on each side closely resembles that of bulk. Similar to the DFT-NEGF formalism we define all atoms in between the leads as C part, marked in gray.

Since we are investigating a nonequilibrium situation, we need to take thermal expansion into account. The temperature difference in the L and R regions leads to a corresponding difference in lattice constants in the electrodes. In order to distribute strain effects equally over the whole junction structure, we therefore determine the volume of the simulation box from the effective lattice constant

$$a_{\mathrm{eff}} = \sqrt[3]{\frac{a_{\mathrm{L}}^3 + a_{\mathrm{R}}^3}{2}}, \tag{9}$$

where a_X are bulk lattice constants at temperature T_X.

In order to calculate a thermal conductance that is comparable to the DFT-NEGF method, the starting point for the C part in the NEMD simulations coincides with the DFT geometry of junction type 1 (JT1), compare Figs. 1 and 2. Large electrodes, oriented along the (111) direction, in the L and R regions are matched to the inner gold pyramid structures. While this procedure ensures geometries in C that are similar to JT1, the junction is likely to be in a different strain situation. This is attributed to differences in equilibrium interatomic distances between DFT and the REAXFF. Additionally, the thermal expansion modifies interatomic equilibrium distances in the NEMD simulations, as discussed in the previous paragraph. The L and R regions in Fig. 1 are five unit cells long, when seen along the transport direction. Regions, where thermostats are applied, are one unit cell thick, and the simulation box is enclosed by two rows of fixed atoms on each side. In the transverse directions we use 12 unit cells, oriented along $(\bar{1}\bar{1}2)$ and $(1\bar{1}0)$ crystallographic directions, respectively. The NEMD junction geometry consists on each side of 384 fixed atoms and 576 atoms in the parts coupled to thermostats. Furthermore, 2880 atoms reside in L and R parts, respectively. With the 4 gold atoms in the pyramidal gold structures of each side and the variable number of atoms in the dithiolated alkane chains C4-C10, this adds up to more than 7700 atoms.

For the integration of Newton's equation of motion, we use the velocity-Verlet algorithm [69]. We perform the NEMD simulations as follows. Apart from the fixed atom regions, random velocities are assigned to all atoms

in the junction to yield a Gaussian distribution centered at 300 K. We start with 1 ns of equilibration with temperatures in the thermostats set to $T_{\rm L} = T_{\rm R} = 300$ K. Next we increase the temperature of the left thermostat $T_{\rm L}$ by the desired temperature difference ΔT to $T_{\rm L} = T_{\rm R} + \Delta T$ over 1 ns. After an additional equilibration time of 1 ns, we perform a time evolution over 4 ns, which constitutes the actual simulation run. The time step chosen for the C4-derived junction is 0.5 fs and 1 fs for C6-C10. In the NEMD simulations the separation between the fixed layers is held constant, i.e. no pulling process is performed.

The thermal conductance is calculated according to

$$\kappa_{\rm pn} = \frac{J}{\Delta T} = \frac{\Delta E}{\Delta t \Delta T}, \tag{10}$$

where $J = \Delta E/\Delta t$ is the steady-state heat current. Overall, $\kappa_{\rm pn}$ is thus obtained from the energy $\Delta E = (-\Delta E_{\rm L} + \Delta E_{\rm R})/2$ supplied to the system by the thermostats L and R per time step Δt, divided by the temperature difference $\Delta T = T_{\rm L} - T_{\rm R}$. Details of the procedure are described in Ref. [68]. In practice, we cumulate the output of the thermostats ΔE over the simulation time $t = N \times \Delta t$ of N MD time steps and extract the heat current J as the slope of a linear fit to $\Delta E^{\rm c}(t) = \sum_{i=1}^{N} \Delta E(i \times \Delta t)$. In the simulations, we print out $\Delta E^{\rm c}(t)$ every 2 ps.

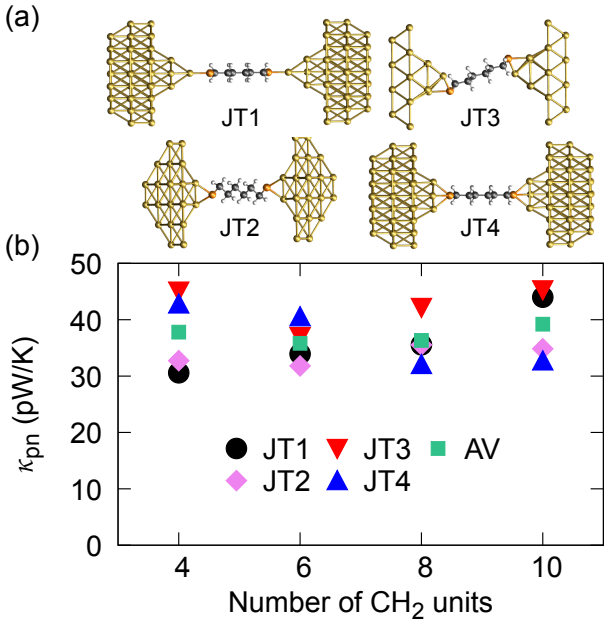

FIG. 2. (a) Different types of junction geometries (JT1-JT4) used for estimating the variability of $\kappa_{\rm pn}$ in dependence on the molecule-electrode contact and the electrode orientation, here shown for C6. (b) Phonon thermal conductance for each junction type, as determined with the DFT-NEGF method, and the average taken over the values of JT1-JT4.

III. VARIABILITY OF THE PHONON THERMAL CONDUCTANCE

Let us in the following discuss the phonon thermal conductance of single-molecule junctions formed from dithiolated alkanes with 4-10 CH_2 units, hereafter named C4-C10, contacted by two gold electrodes. Since the electronic contribution is negligible, the phonon thermal conductance is the relevant property that is measured in novel heat transport experiments [26]. We quantify here the influence that different geometrical variations exert on the phonon thermal conductance of single-molecule junctions. These are the adsorption sites of the sulfur anchors on the gold electrodes and the electrode orientation in Sec. III A, and the influence of gauche defects and strain in Sec. III B. In these two sections, we use the DFT-NEGF approach. Finally, in Sec. III C, we study the effect of thermally induced geometry variations with the help of the NEMD method.

A. Adsorption site and electrode orientation

To better understand the size of variability of the phonon thermal conductance in single-molecule junctions, we start by determining $\kappa_{\rm pn}$ for different junction types with the DFT-NEGF approach. The junctions have been constructed by varying the binding position of the molecular sulfur termini on the gold electrodes as well as the orientation of the metal electrodes with respect to the heat transport direction. Sulfur atoms on both ends are bonded to a single gold tip atom in atop position for JT1, two gold atoms in bridge position for JT2 and JT3, and three gold atoms in a hollow position in JT4. The electrode orientations are (111) for JT1 and JT4, (110) for JT2 and (100) for JT3. The various contact geometries are displayed in Fig. 2(a) for C6. To provide a meaningful comparison among different junction types, JT1-JT4 use fully extended, straight alkane chains. They are built based on the same protocol, which minimizes strain effects by first optimizing the molecule connected to one gold tip structure and then attaching a gold tip on the other side symmetrically and reoptimizing the geometry of the full molecular junction. Within one junction type, all the alkanes of different length show a comparable geometry. The computed phononic thermal conductance is depicted in Fig. 2(b) and found to be in the range of 30 to 50 pW/K with mean values around 35 to 40 pW/K. We note that this data has been presented in "Extended Data Table 1" of Ref. [26]. As discussed there, the thermal conductances are somewhat larger than experimentally detected, since we assume a situation with low mechanical strain. Instead, at the experimentally relevant breaking point, the mechanical tension can pull out gold atoms from the soft electrodes, reducing $\kappa_{\rm pn}$.

The length-independent thermal conductance can be understood by studying the phonon transmission [26, 27],

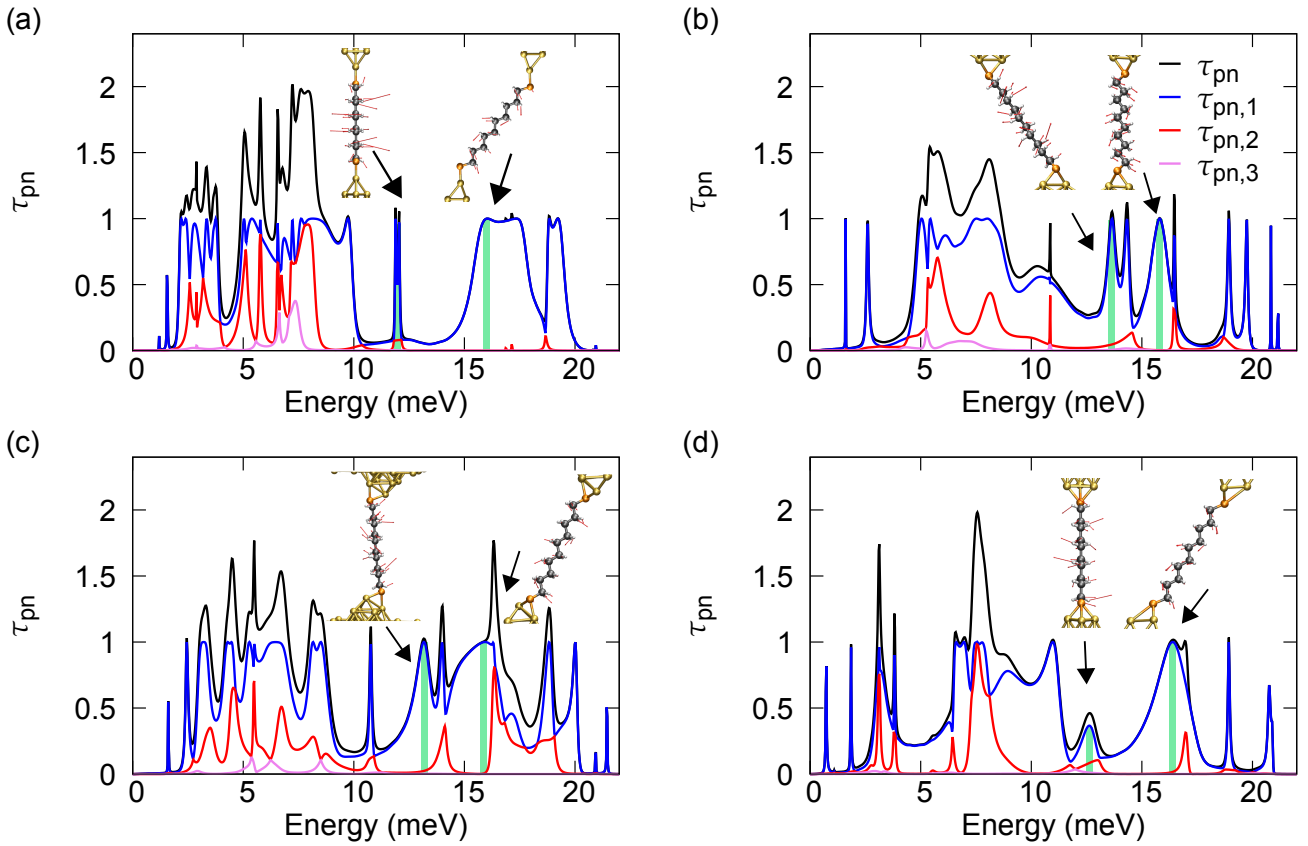

FIG. 3. Total phonon transmission $\tau_{\rm pn}(E)$ resolved into eigenchannel contributions. For JT1-JT4 the transmissions $\tau_{{\rm pn},i}(E)$ of the three most transmissive eigenchannels $i = 1, 2, 3$ are depicted as a function of energy for C10 in panels (a)-(d), respectively. In the inset of each panel, a static picture of the eigenchannel $i = 1$ with the highest transmission is shown for two energies that are indicated by a vertical green line.

which gives the probability of a phonon to be transmitted elastically, i.e. at a specified energy, from one electrode to the other through the alkane molecule. As visible in Fig. 3 for C10, $\tau_{\rm pn}(E)$ exhibits resonances with positions and widths that vary with contact geometry. The transmission vanishes for energies above around $E_{\rm max} = 20$ meV, which corresponds to the highest phonon energies of gold and is comparable to the Debye energy of 15 meV [70]. Through the nearly constant factor $\partial n(E,T)/\partial T$ in Eq. (3), the transmissions in the range from 0 to $E_{\rm max}$ contribute almost equally to $\kappa_{\rm pn}$ at $T = 300$ K. Transmission resonances in this energy interval arise from center-of-mass motions of the alkanes between the gold electrodes or molecular vibrations with low energy. The longer the molecule, the more low-energy vibrational modes will overlap with the phonon density of states of gold, leading to an increasing number of transmission resonances between 0 and $E_{\rm max}$. At the same time transmission resonances become more narrow for the longer alkanes due to a reduced electrode-molecule linewidth broadening. The balance between both effects provides an intuitive explanation for the rather length-independent phonon thermal conductance, as computed here and measured in Ref. [26].

To provide more insight into the origin of the thermal conductance variations, we resolve in Fig. 3 the transmission through C10 for the whole series of junction types into contributions of the three most transmissive eigenchannels. Irrespective of the junction type we observe that two eigenchannels dominate the transmission, while a third one gives only small contributions. With respect to the position and width of the individual transmission resonances, there is a lot of change between different junctions. Since transmission resonances are linked to the vibrational structure of the junctions, they will sensitively depend on the precise contact geometry, in particular the coupling of the molecule to the gold electrodes. As a general feature, we find however that molecular center-of-mass motions tend to yield peaks in the lower part of the energy range between 0 and $E_{\rm max}$, while molecule-internal vibrations are responsible for resonances in the upper part.

To quantify geometry-dependent changes of vibrational modes, we search for eigenchannels with similar shape in the energy range of nonvanishing transmission of Fig. 3. We restrict this analysis to the most trans-

missive first eigenchannel of JT1 at energies of 12.05 and 16.02 meV. On the molecule the vibrations involved can be classified as out-of-plane and in-plane modes, respectively, if we consider the plane spanned by the molecular backbone of sulfur and carbon atoms. Both eigenchannels show two characteristic sign changes when going from one end of the molecule to the other, which we use to identify the corresponding eigenchannels in the other junctions types. As indicated in each panel by insets and vertical green lines, we find the position of the corresponding modes at 13.65 and 15.80 meV for JT2, 13.16 and 16.05 meV for JT3, and 12.78 and 16.43 meV for JT4. While we observe only moderate shifts in energy, the peak widths as well as the peak heights may differ substantially, which exemplifies the crucial impact of contact details on phonon transport.

B. Molecule-internal defects and mechanical strain

In the previous section we focused on the thermal conductance of alkane chains in a straight configuration. However, alkane chains are known to exhibit geometrical defects, which can be thermally activated. In a study of gold-alkane-gold junctions using ab-initio MD simulations [71], the authors related a peak in the histogram of the electrical conductance to these defects. Furthermore they pointed out that upon stretching of the system all defects vanish. For this reason the alkanes are expected to exhibit a straight configuration before breaking of the contact. More recently these defects have been shown to reduce the thermal conductance in comparison to straight chains in a work employing graphene leads [72]. The authors suggested to exploit the mechanism to realize a mechanically driven thermal switch.

To test the influence of molecule-internal disorder on the phonon thermal conductance of C4-C10, we generated chains containing defects by arbitrarily varying torsional angles in the carbon backbone. As described in Sec. III A, we set up the junction in the usual way by first relaxing the twisted chain on top of one electrode and then symmetrically attaching a gold pyramid by point mirroring at the free thiol group. The geometries, which exhibit atomically sharp tips similar to JT1 in Fig. 3, are then stretched to explore their response to different strain conditions. We displace electrodes along the distance vector connecting the gold tip atoms with increments of 0.5 a.u. ≈ 0.265 Å.

Figure 4(a) shows the pulling of the alkane chain with 10 CH_2 units. Initially, the alkane exhibits four gauche defects. Since the gauche defects appear in pairs, the alkane can be described as consisting of three straight segments. In this initial stage the thermal conductance varies smoothly around 20-30 pW/K, while the alkane adjusts continuously to the increasing electrode separation. The region ends at a displacement of 0.24 nm with a jump in κ_{pn}. Here the geometry of the alkane chain changes, two gauche defects vanish, and the remaining pair splits the chain into two straight segments. After two additional displacement steps, leading to a decreased thermal conductance due to the induced strain, an additional jump occurs at a displacement of 0.32 nm. From that moment on the chain is defect-free. Further pulling leads basically to a continuous decrease of the thermal conductance, before the contact finally breaks at an Au-Au bond. A similar behavior is observed for the other chain lengths with 4-8 CH_2 segments, depicted in Fig. 4(b). Again defects in C4-C8 vanish upon pulling, as it is evident from the discontinuous behavior of the thermal conductance. In all examples the thermal conductance of the fully extended configuration is larger than that of geometries with defects. We note that in some cases studied in Fig. 4, Au chains form during the pulling process, namely for the C4, C6 and C8 junctions. The formation of chains depends sensitively on the starting configuration in the DFT simulations, as discussed in Ref. [26].

To better understand the origin of the reduction of κ_{pn} through the torsional gauche defects, we show in Fig. 4(c) the eigenchannel-resolved transmission of three examples with 4, 2, and 0 defects. The geometries of the junctions are depicted as insets, and their thermal conductance values are indicated by arrows and labeled by increasing displacement as D1, D2 and D3 in Fig. 4(a). In the two examples with defects, D1 and D2, phonons within a different energy range are responsible for the reduced conductance as compared to D3. In D1 this energy range is located at about 13-17 meV, for D2 the reduced transmission results from around 4-7 meV. This is particularly evident by analyzing the cumulative thermal conductance. Here, the curves D1 and D3 almost coincide up to an energy of around 13 meV but deviate above. A comparison of D2 and D3, on the other hand, reveals the main difference to start occurring around 4 meV, whereas after 7 meV the offset in $\kappa_{\mathrm{pn}}^{\mathrm{c}}$ stays more or less constant.

Finally, we show in Fig. 4(d) the mean thermal conductance of C4-C10, calculated by averaging over all the thermal conductance values in the contact regime of the pulling process with $\kappa_{\mathrm{pn}} > 0.1$ pW/K. Highest and lowest thermal conductance values in this range are indicated through arrow bars. The mean thermal conductance represents an average over several strain conditions and geometrical configurations, and it shows a nearly length-independent value of 20-30 pW/K. Of course, the starting point for taking the average is somewhat arbitrary in this case, since it is determined by the chosen starting configuration. Interestingly, however, the values predicted for the thermal conductance are similar to what we have computed in Ref. [26] at the point of contact rupture. Indeed, Fig. 4(a) and 4(b) show that junctions with defects in the alkane chain can feature a similar thermal conductance as junctions with straight chains before the point of rupture.

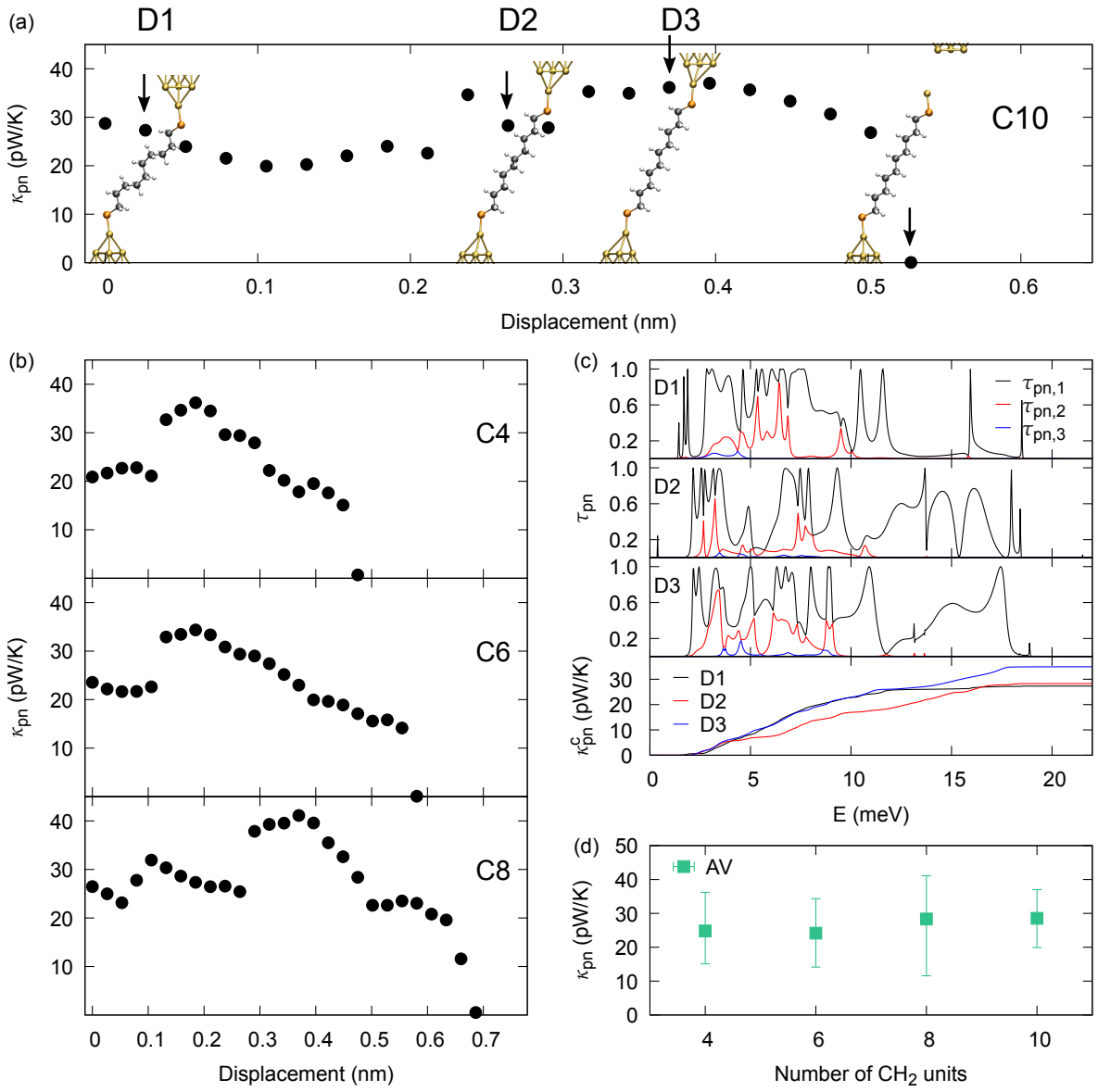

FIG. 4. (a) Phonon thermal conductance κ_{pn} vs. electrode displacement for the C10 chain containing gauche defects. Arrows indicate the thermal conductance of the four geometries visualized in the inset. (b) Corresponding pulling curves for the alkanes C4-C8. (c) Transmission resolved into eigenchannels for the three geometries labeled D1, D2, and D3 in panel (a), together with the cumulative thermal conductance of these junctions. (d) Thermal conductance of C4-C10, calculated as an average over the whole pulling curves shown in panels (a) and (b).

C. Thermally induced geometry changes

To close the analysis, we study temperature-induced geometry changes of single-molecule junctions and their effect on the thermal conductance using NEMD simulations. The chosen interatomic interaction potentials are a crucial point and need to describe reliably the molecular geometry, those of the metallic electrodes and at the same time the metal-molecule interface. Only in this way they can reproduce the vibrational modes that determine the phonon heat transport. As discussed in Sec. II B, we construct junction geometries for the NEMD simulations, see Fig. 1, which show a similar C part as JT1 of Fig. 2, studied with the DFT-NEGF approach. We do so to ensure comparability between both methods. We use the REAXFF of Ref. [67, 73, 74] in our study. It has been optimized for Au-S-C-H systems [74], yields anharmonic interatomic interactions in the whole system, and is able to describe chemical bond formation and dissociation. Overall, we find it to yield reasonable junction geometries.

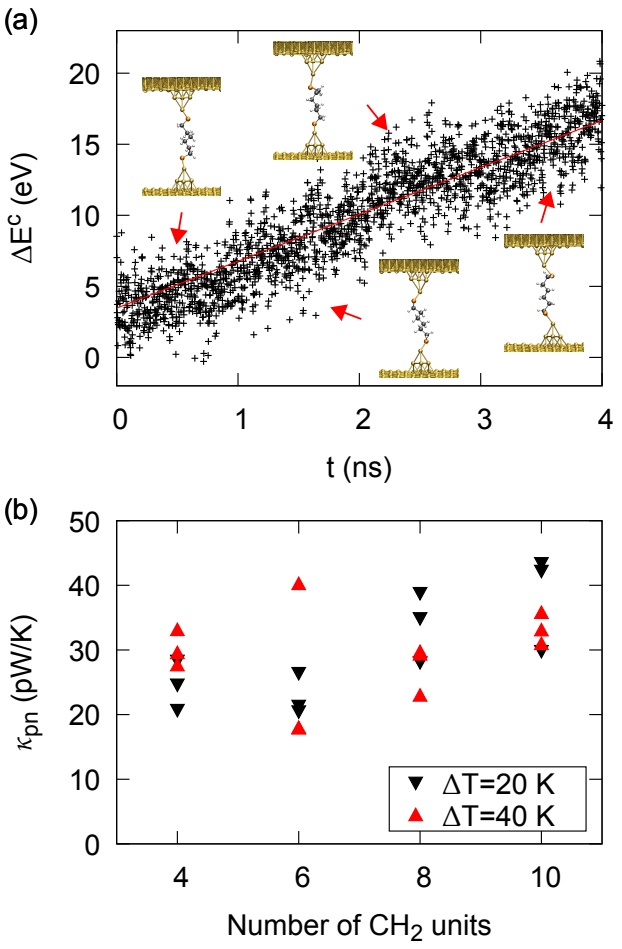

FIG. 5. (a) Cumulated output of the thermostats ΔE^{c} over time for a C6 junction. The red line shows the linear fit used to calculate the thermal current J. For each nanosecond interval a representative geometry is depicted. The non-zero value of ΔE^{c} at $t = 0$ is due to the previous equilibration and temperature rap. (b) Calculated thermal conductance for C4-C10 using temperature gradients of $\Delta T = 20, 40$ K. For each molecule and temperature gradient, data from three different MD runs is displayed. For C6 at $\Delta T = 40$ K two points fall together onto the the low thermal conductance value of around 18 pW/K.

In Fig. 5(a) the cumulated output of the thermostats is displayed as a function of simulation time for a C6 junction. As explained in Sec. II B, we calculate the thermal conductance as the slope of the linear fit, indicated by the red line in Fig. 5(a), divided by the applied temperature difference ΔT, see Eq. (10). It is visible that the output of the thermostats show fluctuations on the order of roughly ± 5 eV. Let us note that ΔE^{c} is an extensive quantity that is proportional to the number of atoms in the regions coupled to the thermostats, and it thus amounts only to ± 8.7 meV/atom. For each interval of a nanosecond simulation time, we show a sample geometry as an inset. Interestingly, apart from the extended chain at the start the alkanes can exhibit different geometrical defects. Temperature fluctuations in the large atom reservoirs in the L and R regions in Fig. 1 lead to an effective modulation of the electrode separation in the C part, which can stretch or squeeze the molecule. The thermal conductance at ambient temperatures arises thus as an average over geometrical configurations, including chains with and without defects. Although shown here only for C6, this holds also for the other molecules.

The thermal conductance for two different temperature differences $\Delta T = 20, 40$ K is plotted in Fig. 5(b) for C4-C10. First of all we note that there is no significant difference related to the applied temperature gradient, meaning that we are in the linear-response regime. Overall the conductances range from 20-40 pW/K. This is somewhat smaller than the thermal conductance determined for the straight alkane chains in the different geometries studied in Fig. 2. In particular, it is lower than the conductances of JT1, from which the NEMD geometries are derived and which we predict to lie between 30 and 45 pW/K. Conversely, the results are in good agreement with the values of κ_{pn}, sampled in the pulling curves that started from defective chains in Sec. III B. For C10 we observe that due to the mentioned mismatch of interatomic distances between DFT and the REAXFF at finite temperature, the geometry at one side changes from an atomically sharp tip to a blunt shape. This corresponds to a higher stress configuration of the alkane chain, or, in analogy with the DFT studies, to a lower probability of defect formation. Indeed, κ_{pn} for C10 is larger than for the other molecules in the NEMD study and in closer agreement with the DFT results of the straight chain.

Overall, we find a good agreement between DFT-NEGF and NEMD methods for the thermal conductance. While the results of both approached will depend on the chosen exchange correlation potential and the selected force field, the consistency indicates that in these single-molecule nanojunctions, anharmonic effects are weak. For this reason, vibrations in the C part behave like waves that proceed elastically through the system at a fixed energy. Since relaxation of energy and dephasing will happen inside the metal reservoirs, the phonon heat transport over the nanoconstriction can also be characterized as phase-coherent.

IV. CONCLUSIONS

In this paper, we presented a comprehensive overview of variations in the phonon thermal conductance of alkane single-molecule junctions at room temperature. For this purpose, we used different methods: A combination of DFT and NEGF to study the thermal conductance in the phase-coherent, harmonic regime and an approach based on classical NEMD to include the effects of temperature and anharmonicity. Since we have shown in Ref. [26] that the electronic contribution to the ther-

mal conductance plays no role for C4 and longer alkanes, the phonon thermal conductance is equivalent to the full thermal conductance apart from radiative effects. Due to the particular measurement scheme, established in Ref. [26], where the molecular junctions spontaneously break at a fixed electrode separation, radiative contributions cancel out and the phonon thermal conductance can thus be uniquely identified.

As the first point, we estimated the variations of κ_{pn} due to different binding positions of sulfur anchors to the gold electrodes, including atop, bridge or hollow positions, as well as due to the orientation of the leads, examining alignments of (111), (110) and (100) crystal directions with the transport direction. These simulations were done with extended alkane chains and the DFT-NEGF method. We found the average thermal conductance to be independent of length within a range of 35-40 pW/K with variations on the order of ± 5 pW/K. By studying the eigenchannel-resolved phonon transmission, we could identify peaks originating from similar molecular vibrations. This served to demonstrate the sensitivity of individual modes to the precise contact geometry. Next, we looked at the influence of molecule-internal disorder. For this purpose, we generated a set of junction geometries, where the alkane contains at least one gauche defect. Subsequently, we varied the distance between the electrodes to investigate the response of the defects to different strain conditions and the impact on heat flow. Consistently, we found in all of the examples that the defects vanish with increased lead separation. Furthermore, in all cases the thermal conductance of the defective chain was reduced in comparison to the defect-free chain. The cumulated conductance revealed that no specific modes within a particular energy range are responsible for the reduction. By averaging over the set of geometries in the conductance-distance curve, we estimated an average κ_{pn} within a range of 20-30 pW/K. Finally, we calculated the room-temperature conductance within the framework of NEMD. While we did not pull the junction, the use of large reservoirs of gold atoms in the electrodes led to thermally induced modulations of the electrode separation. These displacement fluctuations caused a spontaneous appearance or vanishing of molecule-internal defects within the simulation time. With the NEMD method we computed a thermal conductance for C4-C10 in the range of 20-40 pW/K, which is consistent with the previous DFT-NEGF approach.

We note that our NEMD simulations have important implications for using molecule-internal disorder to tune the thermal conductance [72]. If the time to measure the thermal conductance is faster than the transition between different molecular structures, they will be identified in thermal conductance measurements. In the opposite limit, the thermal conductance will appear as an average over structures with straight or defective chains. This latter case is the experimentally relevant situation, since measurements need to average over many seconds to reveal a signal [26], while our simulations show that gauche defects appear and vanish on picosecond time scales. This kind of average due to a low time resolution of measurements was considered in Ref. [72] for graphene electrodes, which show a highest phonon energy of around 185 meV as compared to the 20 meV of Au studied here. The thermal average over different molecular configurations is expected to result in a rather continuous mechanical tuning of the phonon heat transport, and the corresponding increase in thermal conductance due to an increasingly extended alkane would be overlaid by a weakly decreasing radiative heat transport contribution with increasing electrode separation for our three-dimensional metal electrodes [29].

In summary, our study reveals that the thermal conductance of molecular junctions depends crucially on the strain state and is sensitive to the precise atomic configuration. While the heat conductance value will depend on the exchange-correlation functional or force field parametrization used in the DFT-NEGF and NEMD approaches, the consistency of results is reassuring. It confirms that anharmonic effects due to phonon-phonon scattering, taken into account in the NEMD method, do not play a major role in these molecular junctions containing only short molecules. In this sense we identify phonon transport to be elastic and phase-coherent. Since the phonon transport through single-molecule junctions is now experimentally accessible [26], we hope to guide and stimulate future experiments with our study.

V. ACKNOWLEDGMENTS

J.C.K. and F.P. thank P. Reddy, E. Meyhofer, J. C. Cuevas, D. Möhrle, and A. Irmler for inspiring discussions on this project. In addition, both authors gratefully acknowledge funding from the Carl Zeiss foundation, the Junior Professorship Program of the Ministry of Science, Research and the Arts of the state of Baden Württemberg, and the Collaborative Research Center (SFB) 767 of the German Research Foundation (DFG). An important part of the numerical modeling was carried out on the computational resources of the bwHPC program, namely the bwUniCluster and the JUSTUS HPC facility.

[1] A. Aviram and M. A. Ratner, "Molecular rectifiers," Chem. Phys. Lett. **29**, 277 (1974).

[2] M. A. Reed, C. Zhou, C. J. Muller, T. P. Burgin, and J. M. Tour, "Conductance of a molecular junction," Science **278**, 252 (1997).

[3] R. H. M. Smit, Y. Noat, C. Untiedt, N. D. Lang, M. C. van Hemert, and J. M. van Ruitenbeek, "Measurement of the conductance of a hydrogen molecule," Nature **419**,

906 (2002).
[4] A. Nitzan and M. A. Ratner, "Electron transport in molecular wire junctions," Science **300**, 1384 (2003).
[5] B. Xu and N. J. Tao, "Measurement of single-molecule resistance by repeated formation of molecular junctions," Science **301**, 1221 (2003).
[6] P. Reddy, S.-Y. Jang, R. A. Segalman, and A. Majumdar, "Thermoelectricity in molecular junctions," Science **315**, 1568 (2007).
[7] L. Cui, R. Miao, K. Wang, D. Thompson, L. A. Zotti, J. C. Cuevas, E. Meyhofer, and P. Reddy, "Peltier cooling in molecular junctions," Nat. Nanotechnol. **13**, 122 (2018).
[8] W. Lee, K. Kim, W. Jeong, L. A. Zotti, F. Pauly, J. C. Cuevas, and P. Reddy, "Heat dissipation in atomic-scale junctions," Nature **498**, 209 (2013).
[9] M. H. Garner, H. Li, Y. Chen, T. A. Su, Z. Shangguan, D. W. Paley, T. Liu, F. Ng, H. Li, S. Xiao, C. Nuckolls, L. Venkataraman, and G. C. Solomon, "Comprehensive suppression of single-molecule conductance using destructive σ-interference," Nature **558**, 415 (2018).
[10] R. Miao, H. Xu, M. Skripnik, L. Cui, K. Wang, K. G. L. Pedersen, M. Leijnse, F. Pauly, K. Wärnmark, E. Meyhofer, P. Reddy, and H. Linke, "Influence of quantum interference on the thermoelectric properties of molecular junctions," Nano Lett. **18**, 5666 (2018).
[11] D. Djukic and J. M. van Ruitenbeek, "Shot noise measurements on a single molecule," Nano Lett. **6**, 789 (2006).
[12] M. A. Karimi, S. G. Bahoosh, M. Herz, R. Hayakawa, F. Pauly, and E. Scheer, "Shot noise of 1,4-benzenedithiol single-molecule junctions," Nano Lett. **16**, 1803 (2016).
[13] O. S. Lumbroso, L. Simine, A. Nitzan, D. Segal, and O. Tal, "Electronic noise due to temperature differences in atomic-scale junctions," Nature **562**, 240 (2018).
[14] I. Baldea, *Molecular Electronics: An Experimental and Theoretical Approach* (Pan Stanford Publishing, Singapore, 2016).
[15] J. C. Cuevas and E. Scheer, *Molecular Electronics: An Introduction to Theory and Experiment*, 2nd ed. (World Scientific, Singapore, 2017).
[16] K. Moth-Poulsen, *Handbook of Single-Molecule Electronics* (Pan Stanford Publishing, Singapore, 2016).
[17] T. Hines, I. Diez-Perez, J. Hihath, H. Liu, Z.-S. Wang, J. Zhao, G. Zhou, K. Müllen, and N. Tao, "Transition from tunneling to hopping in single molecular junctions by measuring length and temperature dependence," J. Am. Chem. Soc. **132**, 11658 (2010).
[18] L. Venkataraman, J. E. Klare, C. Nuckolls, M. S. Hybertsen, and M. L. Steigerwald, "Dependence of single-molecule junction conductance on molecular conformation," Nature **442**, 904 (2006).
[19] A. Mishchenko, D. Vonlanthen, V. Meded, M. Bürkle, C. Li, I. V. Pobelov, A. Bagrets, J. K. Viljas, F. Pauly, F. Evers, M. Mayor, and T. Wandlowski, "Influence of conformation on conductance of biphenyl-dithiol single-molecule contacts," Nano Lett. **10**, 156 (2010).
[20] Y. S. Park, A. C. Whalley, M. Kamenetska, M. L. Steigerwald, M. S. Hybertsen, C. Nuckolls, and L. Venkataraman, "Contact chemistry and single-molecule conductance: A comparison of phosphines, methyl sulfides, and amines," J. Am. Chem. Soc. **129**, 15768 (2007).
[21] E. Leary, A. La Rosa, M. T. González, G. Rubio-Bollinger, N. Agraït, and N. Martín, "Incorporating single molecules into electrical circuits. The role of the chemical anchoring group," Chem. Soc. Rev. **44**, 920 (2015).
[22] L. Venkataraman, Y. S. Park, A. C. Whalley, C. Nuckolls, M. S. Hybertsen, and M. L. Steigerwald, "Electronics and chemistry: Varying single-molecule junction conductance using chemical substituents," Nano Lett. **7**, 502 (2007).
[23] J. Vacek, J. V. Chocholoušová, I. G. Stará, I. Starý, and Y. Dubi, "Mechanical tuning of conductance and thermopower in helicene molecular junctions," Nanoscale **7**, 8793 (2015).
[24] D. Stefani, K. J. Weiland, M. Skripnik, C. Hsu, M. L. Perrin, M. Mayor, F. Pauly, and H. S. J. van der Zant, "Large conductance variations in a mechanosensitive single-molecule junction," Nano Lett. **18**, 5981 (2018).
[25] D. Dulić, S. J. van der Molen, T. Kudernac, H. T. Jonkman, J. J. D. de Jong, T. N. Bowden, J. van Esch, B. L. Feringa, and B. J. van Wees, "One-way optoelectronic switching of photochromic molecules on gold," Phys. Rev. Lett. **91**, 207402 (2003).
[26] L. Cui, S. Hur, Z. A. Akbar, J. C. Klöckner, W. Jeong, F. Pauly, S.-Y. Jang, P. Reddy, and E. Meyhofer, "Thermal conductance of single-molecule junctions," Nature **572**, 628 (2019).
[27] J. C. Klöckner, M. Bürkle, J. C. Cuevas, and F. Pauly, "Length dependence of the thermal conductance of alkane-based single-molecule junctions: An ab initio study," Phys. Rev. B **94**, 205425 (2016).
[28] J. C. Klöckner, J. C. Cuevas, and F. Pauly, "Tuning the thermal conductance of molecular junctions with interference effects," Phys. Rev. B **96**, 245419 (2017).
[29] J. C. Klöckner, R. Siebler, J. C. Cuevas, and F. Pauly, "Thermal conductance and thermoelectric figure of merit of C_{60}-based single-molecule junctions: Electrons, phonons, and photons," Phys. Rev. B **95**, 245404 (2017).
[30] T. Markussen, "Phonon interference effects in molecular junctions," J. Chem. Phys. **139**, 244101 (2013).
[31] Q. Li, M. Strange, I. Duchemin, D. Donadio, and G. C. Solomon, "A strategy to suppress phonon transport in molecular junctions using π-stacked systems," J. Phys. Chem. C **121**, 7175 (2017).
[32] M. Famili, I. Grace, H. Sadeghi, and C. J. Lambert, "Suppression of phonon transport in molecular Christmas trees," Chem. Phys. Chem. **18**, 1234 (2017).
[33] R. Y. Wang, R. A. Segalman, and A. Majumdar, "Room temperature thermal conductance of alkanedithiol self-assembled monolayers," Appl. Phys. Lett. **89**, 173113 (2006).
[34] Z. Wang, J. A. Carter, A. Lagutchev, Y. K. Koh, N.-H. Seong, D. G. Cahill, and D. D. Dlott, "Ultrafast flash thermal conductance of molecular chains," Science **317**, 787 (2007).
[35] T. Meier, F. Menges, P. Nirmalraj, H. Hölscher, H. Riel, and B. Gotsmann, "Length-dependent thermal transport along molecular chains," Phys. Rev. Lett. **113**, 060801 (2014).
[36] M. Bürkle, T. J. Hellmuth, F. Pauly, and Y. Asai, "First-principles calculation of the thermoelectric figure of merit for [2,2]paracyclophane-based single-molecule junctions," Phys. Rev. B **91**, 165419 (2015).
[37] J. C. Klöckner and F. Pauly, unpublished.

[38] L. G. C. Rego and G. Kirczenow, "Quantized thermal conductance of dielectric quantum wires," Phys. Rev. Lett. **81**, 232 (1998).

[39] N. Mingo and L. Yang, "Phonon transport in nanowires coated with an amorphous material: An atomistic Green's function approach," Phys. Rev. B **68**, 245406 (2003).

[40] T. Yamamoto and K. Watanabe, "Nonequilibrium Green's function approach to phonon transport in defective carbon nanotubes," Phys. Rev. Lett. **96**, 255503 (2006).

[41] F. Pauly, J. K. Viljas, U. Huniar, M. Häfner, S. Wohlthat, M. Bürkle, J. C. Cuevas, and G. Schön, "Cluster-based density-functional approach to quantum transport through molecular and atomic contacts," New J. Phys. **10**, 125019 (2008).

[42] F. Guinea, C. Tejedor, F. Flores, and E. Louis, "Effective two-dimensional Hamiltonian at surfaces," Phys. Rev. B **28**, 4397 (1983).

[43] J. C. Klöckner, J. C. Cuevas, and F. Pauly, "Transmission eigenchannels for coherent phonon transport," Phys. Rev. B **97**, 155432 (2018).

[44] TURBOMOLE, http://www.turbomole.com.

[45] P. Deglmann, F. Furche, and R. Ahlrichs, "An efficient implementation of second analytical derivatives for density functional methods," Chem. Phys. Lett. **362**, 511 (2002).

[46] P. Deglmann, K. May, F. Furche, and R. Ahlrichs, "Nuclear second analytical derivative calculations using auxiliary basis set expansions," Chem. Phys. Lett. **384**, 103 (2004).

[47] J. P. Perdew and Y. Wang, "Accurate and simple analytic representation of the electron-gas correlation energy," Phys. Rev. B **45**, 13244 (1992).

[48] J. P. Perdew, K. Burke, and M. Ernzerhof, "Generalized gradient approximation made simple," Phys. Rev. Lett. **77**, 3865 (1996).

[49] F. Weigend and R. Ahlrichs, "Balanced basis sets of split valence, triple zeta valence and quadruple zeta valence quality for H to Rn: Design and assessment of accuracy," Phys. Chem. Chem. Phys. **7**, 3297 (2005).

[50] F. Weigend, "Accurate Coulomb-fitting basis sets for H to Rn," Phys. Chem. Chem. Phys. **8**, 1057 (2006).

[51] P. K. Schelling, S. R. Phillpot, and P. Keblinski, "Comparison of atomic-level simulation methods for computing thermal conductivity," Phys. Rev. B **65**, 144306 (2002).

[52] F. Müller-Plathe, "A simple nonequilibrium molecular dynamics method for calculating the thermal conductivity," J. Chem. Phys. **106**, 6082 (1997).

[53] G. Ciccotti and A. Tenenbaum, "Canonical ensemble and nonequilibrium states by molecular dynamics," J. Stat. Phys. **23**, 767 (1980).

[54] E. S. Landry and A. J. H. McGaughey, "Thermal boundary resistance predictions from molecular dynamics simulations and theoretical calculations," Phys. Rev. B **80**, 165304 (2009).

[55] Y. Chalopin, K. Esfarjani, A. Henry, S. Volz, and G. Chen, "Thermal interface conductance in Si/Ge superlattices by equilibrium molecular dynamics," Phys. Rev. B **85**, 195302 (2012).

[56] J.-L. Barrat and F. Chiaruttini, "Kapitza resistance at the liquid-solid interface," Mol. Phys. **101**, 1605 (2003).

[57] S. Merabia and K. Termentzidis, "Thermal conductance at the interface between crystals using equilibrium and nonequilibrium molecular dynamics," Phys. Rev. B **86**, 094303 (2012).

[58] D. P. Sellan, E. S. Landry, J. E. Turney, A. J. H. McGaughey, and C. H. Amon, "Size effects in molecular dynamics thermal conductivity predictions," Phys. Rev. B **81**, 214305 (2010).

[59] Z. Liang and P. Keblinski, "Finite-size effects on molecular dynamics interfacial thermal-resistance predictions," Phys. Rev. B **90**, 075411 (2014).

[60] Z. Wang and X. Ruan, "On the domain size effect of thermal conductivities from equilibrium and nonequilibrium molecular dynamics simulations," J. Appl. Phys. **121**, 044301 (2017).

[61] S. Plimpton, "Fast parallel algorithms for short-range molecular dynamics," J. Comput. Phys. **117**, 1 (1995).

[62] T. Luo and J. R. Lloyd, "Non-equilibrium molecular dynamics study of thermal energy transport in Au-SAM-Au junctions," Int. J. Heat Mass Transf. **53**, 1 (2010).

[63] J. Soussi, S. Volz, B. Palpant, and Y. Chalopin, "A detailed microscopic study of the heat transfer at a water gold interface coated with a polymer," Appl. Phys. Lett. **106**, 093113 (2015).

[64] W.-L. Ong, S. Majumdar, J. A. Malen, and A. J. H. McGaughey, "Coupling of organic and inorganic vibrational states and their thermal transport in nanocrystal arrays," J. Phys. Chem. C **118**, 7288 (2014).

[65] S. Majumdar, J. A. Sierra-Suarez, S. N. Schiffres, W.-L. Ong, C. F. Higgs, A. J. H. McGaughey, and J. A. Malen, "Vibrational mismatch of metal leads controls thermal conductance of self-assembled monolayer junctions," Nano Lett. **15**, 2985 (2015).

[66] M. F. Russo and A. C. T. van Duin, "Atomistic-scale simulations of chemical reactions: Bridging from quantum chemistry to engineering," Nucl. Instrum. Methods Phys. Res., Sect. B **269**, 1549 (2011).

[67] T. P. Senftle, S. Hong, M. M. Islam, S. B. Kylasa, Y. Zheng, Y. K. Shin, C. Junkermeier, R. Engel-Herbert, M. J. Janik, H. M. Aktulga, T. Verstraelen, A. Grama, and A. C. T. van Duin, "The ReaxFF reactive force-field: development, applications and future directions," njp Comput. Mater. **2**, 15011 (2016).

[68] D. O. Möhrle, F. Müller, M. Matt, P. Nielaba, and F. Pauly, "Statistical analysis of electronic and phononic transport simulations of metallic atomic contacts," Phys. Rev. B **100**, 125433 (2019).

[69] W. C. Swope, H. C. Andersen, P. H. Berens, and K. R. Wilson, "A computer simulation method for the calculation of equilibrium constants for the formation of physical clusters of molecules: Application to small water clusters," J. Chem. Phys. **76**, 637 (1982).

[70] N. W. Ashcroft and N. Mermin, *Solid State Physics* (Hartcourt, Orlando, 1976).

[71] M. Paulsson, C. Krag, T. Frederiksen, and M. Brandbyge, "Conductance of alkanedithiol single-molecule junctions: A molecular dynamics study," Nano Lett. **9**, 117 (2009).

[72] Q. Li, I. Duchemin, S. Xiong, G. C. Solomon, and D. Donadio, "Mechanical tuning of thermal transport in a molecular junction," J. Phys. Chem. C **119**, 24636 (2015).

[73] T. T. Järvi, A. C. T. van Duin, K. Nordlund, and W. A. Goddard, "Development of interatomic ReaxFF potentials for Au-S-C-H systems," J. Phys. Chem. A **115**, 10315 (2011).

[74] G.-T. Bae and C. M. Aikens, "Improved ReaxFF force field parameters for Au-S-C-H systems," J. Phys. Chem. A **117**, 10438 (2013).